



Fe-substituted $10\text{Al}_2\text{O}_3 \cdot 2\text{B}_2\text{O}_3$ as a multifunctional support for automotive Pd catalysts

Keita Ikeue^a, Kazuma Watanabe^a, Takayuki Minekishi^a, Ayaka Imamura^a,
Takahiro Sato^b, Yuki Nagao^b, Yunosuke Nakahara^b, Masato Machida^{a,*}

^a Department of Applied Chemistry and Biochemistry, Graduate School of Science and Technology, Kumamoto University, 2-39-1 Kurokami, Chuo-ku, Kumamoto 860-8555, Japan

^b Catalysts Strategic Division, Engineered Materials Sector, Mitsui Mining and Smelting Co., Ltd., 1013-1 Ageosimo, Ageo 362-0025, Japan

ARTICLE INFO

Article history:

Received 1 November 2012

Accepted 3 April 2013

Available online 10 April 2013

Keywords:

Aluminum oxide borate

Three-way catalyst

Palladium

Oxygen storage

ABSTRACT

Partial substitution of various transition metals for Al in $10\text{Al}_2\text{O}_3 \cdot 2\text{B}_2\text{O}_3$ ($\text{Al}_{20}\text{B}_4\text{O}_{36}$, 10A2B) was studied to use as a thermostable support for Pd catalysts. Fe-substitution afforded the formation of solid solutions in the range of $x \leq 1.5$ in $\text{Fe}_x\text{Al}_{20-x}\text{B}_4\text{O}_{36}$ (Fe-10A2B) without impurities. The DFT calculations confirmed that Fe-substitution was most likely to occur on the 5-coordinated Al site and predicted a shorter Fe–O distances of 1.84–2.05 Å compared to 1.94 and 2.12 Å in Fe_2O_3 , in accordance with Fe–K edge EXAFS results. Fe-substitution improved the catalytic NO conversion in a rich region ($A/F < 14.6$), because CO–H₂O and subsequent NO–H₂ reactions were accelerated. The redox between Fe^{3+} and Fe^{2+} in Fe-10A2B generated the oxygen storage capacity (OSC), which yielded an efficient buffering effect on air-to-fuel (A/F) fluctuation in a simulated exhaust gas stream with lean/rich perturbation. These results suggest that Fe-10A2B is expected to be used as a multifunctional support material for Pd catalysts in automotive three-way catalysts.

© 2013 Elsevier B.V. All rights reserved.

1. Introduction

We have recently demonstrated that aluminum oxide borate, $10\text{Al}_2\text{O}_3 \cdot 2\text{B}_2\text{O}_3$ ($\text{Al}_{20}\text{B}_4\text{O}_{36}$, 10A2B), is a potential material as a novel automotive catalyst support having high specific surface area and thermal stability [1]. The crystal structure of 10A2B is described as one of mullite analogs consisting of AlO_6 octahedra, irregular AlO_5 polyhedra, AlO_4 tetrahedra and planar BO_3 triangles (see Fig. 2) [2–5]. Because of the planar BO_3 unit, which has a pronounced effect in lowering the bulk density, 10A2B forms porous microstructures suitable for catalytic applications. However, the previous catalytic studies have been limited to the work reported by Garbowski et al. [6] and our previous work [1]. Garbowski et al. [6] have reported that Pd/10A2B showed a much higher stability than Pd/ Al_2O_3 in the high temperature methane combustion, but neither analyses of the metal–support interaction nor other catalytic applications have been reported. We have demonstrated that the most beneficial point of 10A2B compared to gamma- Al_2O_3 is tolerance to water vapor at high temperatures, which is an important factor as automotive catalyst support materials [1]. The addition of the alkaline earth and rare earth elements such as Ba achieved the most efficient stability against Pd sintering and the lowest light-off

temperatures for a stoichiometric NO–CO– C_3H_6 – O_2 gas stream. The high basicity of Ba in comparison with other additives would play a key role in the enhancement of NO reactivity and the reduction of self-poisoning effect of C_3H_6 under the rich condition ($A/F < 14.6$).

The present study was concentrated on cation-substitution as another possible structural modification of 10A2B toward further enhancement of catalytic properties. Cation-substitution is of great interest because its validity has already been demonstrated in a series of hexaaluminate catalysts for high-temperature methane combustion [7–13]. Partial replacement of Al in hexaaluminate ($\text{M}^{2+}\text{Al}_{12}\text{O}_{19}$ and/or $\text{M}^{3+}\text{Al}_{11}\text{O}_{18}$) by a transition metal (Cr, Mn, Fe, Co and Ni) yields considerable catalytic activity for methane combustion without losing surface area and thermal stability. The catalytic activities of substituted hexaaluminates are connected to the smooth change in oxidation state of each transition metal, being highest in the case of Mn. By contrast, cation-substituted 10A2B compounds have not been investigated as catalytic materials.

The present study aims to prepare and characterize the novel cation-substituted 10A2B as support materials for automotive Pd catalysts. Fe capable of highest degree of substitution was mainly studied from viewpoints the crystal structure and the local structure. A particular attention has been paid toward the influence of the Fe-substitution on the catalytic properties of Pd, which was evaluated using simulated NO–CO– C_3H_6 – O_2 gas mixtures and their elemental reactions in a light-off mode. A modulated air-to-fuel

* Corresponding author. Tel.: +81 96 342 3651; fax: +81 96 342 3651.
E-mail address: machida@kumamoto-u.ac.jp (M. Machida).

ratio (A/F) mode was also applied to study catalytic activities under rich or lean conditions and oxygen release/storage properties.

2. Experimental

2.1. Catalyst preparation

$\text{Al}_{20}\text{B}_4\text{O}_{36}$ (10A2B) and its cation-substituted compounds, $\text{M}_x\text{Al}_{20-x}\text{B}_4\text{O}_{36}$ (M-10A2B) were prepared by reverse coprecipitation method [1]. The aqueous solution containing nitrates of M (M = Mn, Fe, Co, Ni, Cu, Mg, Ga) and Al and H_3BO_3 (Wako Pure Chemicals) with a molar ratio of M:Al:B = $x:20-x:4$ was added dropwise to 3 mol/L $(\text{NH}_4)_2\text{HCO}_3$ under vigorous stirring. The addition of the mixed solution was stopped when the pH reached 7. The precipitate thus formed was evaporated to dryness and calcined at 300 °C and finally at 1000 °C for 5 h in air. Supported Pd catalysts (0.4 wt% as Pd metal) were prepared by impregnation of an aqueous solution of $\text{Pd}(\text{NO}_3)_2$ (Tanaka Precious Metals), followed by drying and calcination at 600 °C for 3 h in air. The catalysts as prepared and thermally aged in a stream of 10% H_2O /air at 900 °C for 25 h were used for catalytic tests as described below.

2.2. Characterization

Powder X-ray diffraction (XRD) measurement was performed using monochromated $\text{CuK}\alpha$ radiation (30 kV, 20 mA, Rigaku Multiflex). The content of Pd was determined by X-ray fluorescence measurement (Rigaku EDXL300). Metal dispersion of Pd was measured by CO chemisorption using a commercial instrument (Bel-cat, Bel Japan, Inc.) at 50 °C after reduction at 400 °C in H_2 . BET surface area (S_{BET}) was calculated from N_2 adsorption isotherms measured at 77 K (Belsorp, Bel Japan, Inc.).

X-ray absorption spectra of Fe K-edge were measured on the BL-7C station of Photon Factory (PF), High Energy Accelerator Research Organization (KEK) at Tsukuba (Proposal No. 2011G619). A Si (1 1 1) double-crystal monochromator was used. The spectra were recorded at ambient temperature in a transmission mode using an ionization chamber filled with N_2 for an incident beam and another chamber filled with 15% Ar+85% N_2 for a transmitted beam. A reference sample (Fe_2O_3 , 3 mg) was mixed with boron nitride (BN) powders (50 mg) to give an appropriate absorbance at the edge energy, whereas other samples (30 mg) were used without mixing with BN. The XAFS data were processed by a REX 2000 program (Rigaku). EXAFS oscillation was extracted by fitting a cubic spline function through the post edge region. The k^3 -weighted EXAFS oscillation in the 3.0–14.0 \AA^{-1} regions was Fourier transformed. The reference (Fe_2O_3) was used to extract the amplitude and phase shift function for Fe–O shells. Coordination number (CN), interatomic distance (r) and ΔE_0 were fitted and Debye–Waller factors were fixed.

X-band CW-EPR spectra of Fe-10A2B before and after H_2 reduction were measured on a Bruker ESP350E spectrometer equipped with a cylindrical cavity operating at a 100 kHz field modulation. The reduction treatment was carried out in a flow of 1.67% H_2 /He at 700 °C for 5 min and subsequently cooled by liquid He at 20 K, where spectra were recorded.

Dynamic reduction–oxidation behavior was studied by the use of microbalance (TG, Rigaku 8120), which is connected to a dual-gas supplying system. The catalyst (10 mg) was firstly heated in a stream of N_2 up to 800 °C, where the constant weight was attained within 30 min. Then, the gas feed was switched between 1.4% H_2 and 0.7% O_2 balanced by N_2 with recording the catalyst weight at this temperature.

2.3. DFT calculation

Because 10A2B has four different Al sites (see Fig. 2 for detail), the energies of hypothetical Fe incorporation into each sites in $\text{FeAl}_{19}\text{B}_4\text{O}_{36}$ were investigated using computational simulation techniques making use of DFT. The spin-polarized generalized gradient approximation GGA+ U method (U = Hubbard U) electronic calculations were performed with Vienna *Ab initio* Simulation Package (VASP) [14]. Calculations were performed using projector augmented-wave PAW potentials for Fe, Al, B and O atoms. A plane-wave basis set with a cutoff of 520 eV was used. The Perdew–Burke–Ernzerhof GGA was employed for the exchange and correlation functionals. Sums over occupied electronic states were performed using the Monkhorst–Pack scheme [15] on a $4 \times 2 \times 3$ set of a k -point mesh. A simplified GGA+ U method after Dudarev et al. [16] was utilized. The value of U – J (4.3 eV) for Fe 3d channel was adopted from the literature [17]. Unit-cell parameters and atomic coordinates of 10A2B were optimized with the convergence condition of 0.02 eV/Å for an orthorhombic cell. Initial crystallographic parameters used in the optimization were referred from the literature [18].

2.4. Catalytic tests

Catalytic tests were carried out in a flow reactor at atmospheric pressure. 50 mg of catalyst (10–20 mesh) was fixed in a quartz tube (4 mm i.d.) by quartz wool at both ends of the catalyst bed. Temperature dependence of catalytic activity was evaluated by heating the catalyst bed from ambient temperature to 600 °C at a constant rate of 10 °C min^{−1} (light-off mode) while supplying a simulated exhaust gas mixture containing NO (0.050%), CO (0.51%) C_3H_6 (0.039%), O_2 (0.40%) and He (balance) at 100 cm³ min^{−1} ($W/F = 5.0 \times 10^{-4}$ g min cm^{−3}). The gas composition corresponds to the stoichiometric air-to-fuel ratio ($A/F = 14.6$). The effluent gas was analyzed using a Pfeiffer GSD30101 mass spectrometer and a Horiba VA3000 NDIR gas analyzer. Catalytic tests for several elemental reactions such as $\text{CO}-\text{O}_2$, $\text{NO}-\text{CO}$, $\text{C}_3\text{H}_6-\text{O}_2$ and so on were carried out using the same experimental set-up.

Catalytic tests were also carried out under modulating A/F condition ($13.7 \leq A/F \leq 15.1$) at a constant reaction temperature using a simulated exhaust gas mixture containing NO (0.050%), CO (0.51%) C_3H_6 (0.039%), O_2 (0.10–0.80%), H_2O (10%) and He (balance) supplied at 100 cm³ min^{−1} ($W/F = 5.0 \times 10^{-4}$ g min cm^{−3}). In this mode, O_2 concentration in the gas feed was varied with time-on-stream, but concentrations of other gases (NO, CO, C_3H_6 , H_2O) and the rate of total gas feed were fixed at constant. The average rate of A/F scan was set at 2.2 h^{−1}. The value of A/F was calculated from concentrations of each gases in the gas feed as has been reported by Tanaka et al. [19]. The oxygen storage performance was also evaluated in the flow of gas mixtures as above described, but two O_2 gas feeds were switched between 0.83% O_2 ($A/F = 15.0$) and 0.17% O_2 ($A/F = 14.2$) at an interval of 10 s. The A/F value of gas stream at the outlet of the catalyst bed was monitored using Horiba MEXA-730.

3. Results and discussion

3.1. Structure of substituted 10A2B

Fig. 1 shows the XRD patterns of $\text{MAl}_{19}\text{B}_4\text{O}_{36}$ (M = Al, Mn, Fe, Co, Ni, Mg, Ga) as calcined at 1000 °C in air. The pristine compounds (M = Al) consisted of a single phase of 10A2B, the diffraction peaks of which were indexed on the basis of orthorhombic cell with the $\text{Cmc}2_1$ space group. As represented in Fig. 2, the crystal structure of 10A2B is constructed by isolated chains of edge-sharing $\text{Al}(\text{I})\text{O}_6$ octahedra (shown as thick lines) running parallel to the a -axis,

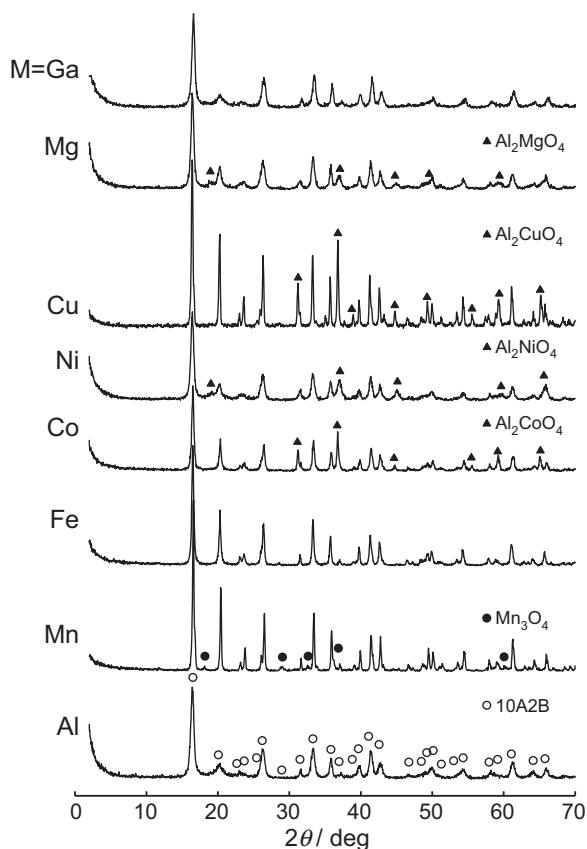


Fig. 1. XRD patterns of products with a nominal composition of $\text{MAI}_{19}\text{B}_4\text{O}_{36}$ (M=10A2B) after calcination at 1000 °C.

which are connected by pairs of irregular edge-sharing $\text{Al}(2)\text{O}_5$ and $\text{Al}(3)\text{O}_5$ polyhedra (shown as thin lines), $\text{Al}(4)\text{O}_4$ tetrahedra (shown as gray lines) and BO_3 triangles [2,3]. These structural units form cylindrical cavities running along the a -axis, which is a primary reason for the lower density, 2.94 g cm^{-3} , compared to those of $\alpha\text{-Al}_2\text{O}_3$ and other transition aluminas ($3.6\text{--}4.0\text{ g cm}^{-3}$). Among cation-substituted compounds, $\text{M}=\text{Mn}, \text{Co}, \text{Ni}, \text{Cu}$ and Mg yielded spinel-type Mn_3O_4 or Al_2MgO_4 as by-products, diffraction intensities of which were dependent on the solubility limit of each cations into the 10A2B phase. Contrary to these divalent cations, no such impurities were detected for trivalent cations, $\text{M}=\text{Ga}$ and Fe , suggesting the formation of solid solutions. This is different from hexaaluminate compounds, which are capable of incorporating various divalent and/or trivalent cations to a larger extent into

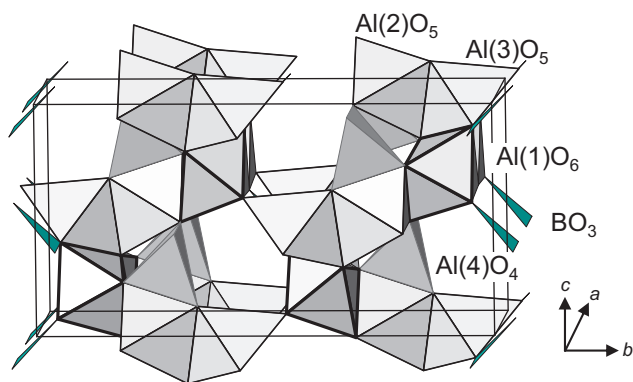


Fig. 2. Crystal structure of $\text{Al}_{20}\text{B}_4\text{O}_{36}$ (10A2B).

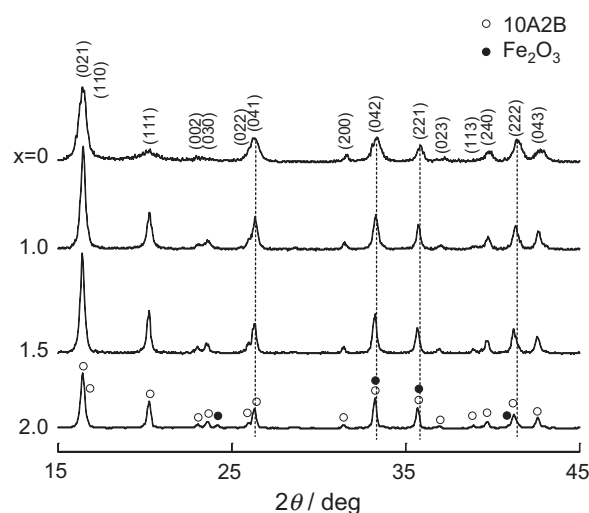


Fig. 3. XRD patterns of products with a nominal composition of $\text{Fe}_x\text{Al}_{20-x}\text{B}_4\text{O}_{36}$ after calcination at 1000 °C.

their spinel-type moiety [7]. 10A2B can therefore incorporate less amounts of transition metal cations than hexaaluminates.

Fig. 3 exhibits the XRD patterns of Fe-substituted 10A2B with different amounts of Fe ($\text{Fe}_x\text{Al}_{20-x}\text{B}_4\text{O}_{36}$, $0 < x \leq 2.0$). With an increase of x , the diffraction peaks shifted to lower 2θ , suggesting the increase of lattice parameters as summarized in Table 1. This is indicative of the occupation of the Al site by Fe^{3+} having a larger ionic radius (Al^{3+} : 0.057 nm , Fe^{3+} 0.067 nm). At $x \geq 1.5$, however, the lattice parameters were almost constant and the deposition of unsubstituted Fe_2O_3 occurred. The solubility limit of Fe in 10A2B is thus determined to be around $x = 1.5$. As shown in Fig. 2, four different Al sites exist in 10A2B. Fe K-edge EXAFS was next measured to determine which Al sites could accommodate Fe. Fig. 4 compares Fe K-edge EXAFS of Fe-10A2B and Fe_2O_3 . When the first and second coordination shells are filtered, the best curve-fitting is obtained and resultant structural parameters including phase shift corrected r -values are shown in Table 2 (see supplementary data for details). Unlike Fe_2O_3 having six Fe–O coordination numbers with 1.94 and 2.12 \AA in the first shell, Fe–O in Fe-10A2B shows smaller coordination number ($\text{CN}=3.3$) and shorter distances ($r=1.88$ and 1.95 \AA). Peaks in the second shell are attributed to Fe–O–Al with $r=2.89$, 3.26 and 3.54 \AA and $\text{CN}=1.4$, 1.2 and 1.5 , respectively. The fitting is not successful when the Fe–O–Fe shells with longer interatomic distances are taken into consideration.

The structure optimization of $\text{FeAl}_{19}\text{B}_4\text{O}_{36}$ with hypothetical Fe incorporation into four different Al sites was carried out by means of DFT calculation. The errors of calculated lattice parameters are within 1.7% compared to the experimental values shown in Table 1. As shown in supplementary data for details, the total energy for each case exhibits the following sequence of increasing values: $\text{Al}(3) < \text{Al}(2) < \text{Al}(1) < \text{Al}(4)$, suggesting that Fe substitution is most likely to occur on the 5-coordinated Al(3) site. Considering the small energy difference between two 5-coordinated sites, Al(2) and Al(3), however, both site may be involved in the Fe substitution process.

Table 1
Lattice parameters of $\text{Fe}_x\text{Al}_{20-x}\text{B}_4\text{O}_{36}$ after calcination at 1000 °C.

x	a/nm	b/nm	c/nm
0	5.662(2)	15.019(8)	7.654(4)
1.0	5.686(2)	15.068(4)	7.707(4)
1.5	5.690(1)	15.076(6)	7.713(2)
2.0	5.686(1)	15.066(4)	7.708(2)

Parameters for an orthorhombic cell with the $\text{Cmc}2_1$ space group are shown.

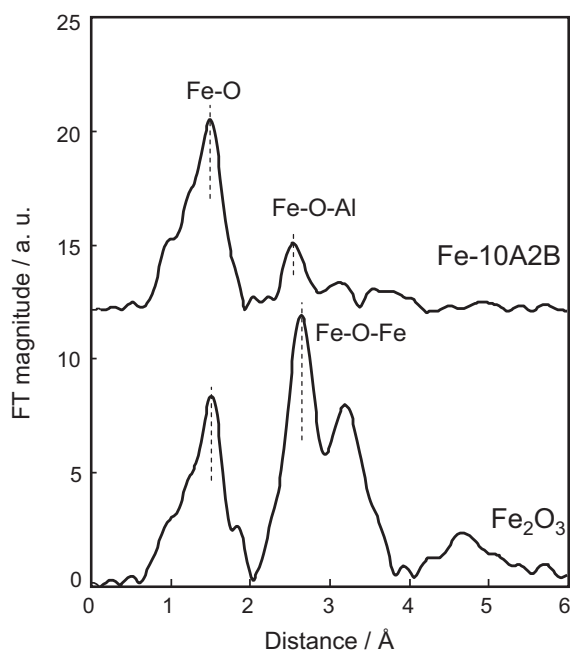


Fig. 4. Fourier transforms of k^3 -weighted Fe K-edge EXAFS for (a) Fe-10A2B and (b) Fe_2O_3 without corrections for phase shifts.

The predicted Fe–O distances, 1.84–2.05 Å, are close to those determined by EXAFS (1.88 and 1.95 Å, Table 2) and smaller than those of Fe_2O_3 (1.94 and 2.12 Å). The highest energy of Fe in 4-coordinated Al(4) should be associated with the stress due to the larger ionic size of Fe^{3+} than Al^{3+} .

3.2. Catalytic property of substituted 10A2B

In the following, we focus on the Fe-10A2B system, which enables the substitution with least amounts of impurities. Table 3 summarizes BET surface area (S_{BET}), metal dispersion and catalytic activity of 0.4 wt% Pd-loaded $\text{Fe}_x\text{Al}_{20-x}\text{B}_4\text{O}_{36}$ before and after thermal aging. Here, metal dispersion is expressed in terms of CO/Pd, which is a molar ratio of CO adsorbed per total Pd loaded, because *in situ* FT-IR measurement detected linear (CO:Pd_{surf} = 1:1) and bridged forms (CO:Pd_{surf} = 1:2 and/or 1:3) of carbonyl species adsorbed onto surface Pd atom (Pd_{surf}) with different contributions. The BET surface areas of 10A2B decreased with an increase of Fe(x). This is one possible reason of lower Pd metal dispersion on Fe-10A2B. The metal dispersion after thermal aging at 900 °C could

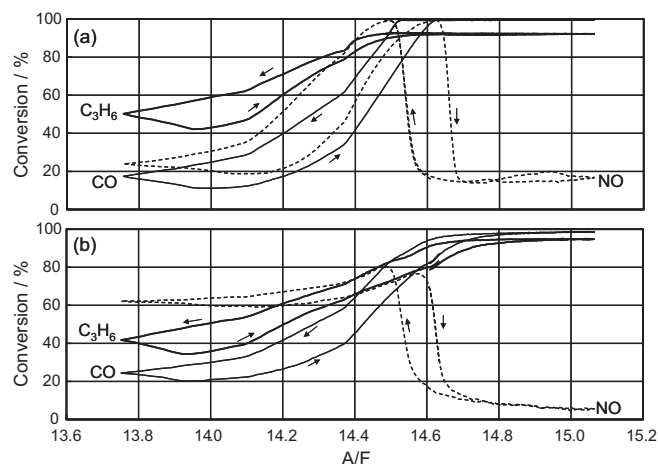


Fig. 5. Catalytic conversion of CO, NO and C_3H_6 at 390 °C under modulated A/F condition in the range $13.7 \leq \text{A/F} \leq 15.1$. (a) Pd/10A2B and (b) Pd/Fe-10A2B. The catalysts were aged at 900 °C for 25 h in 10% $\text{H}_2\text{O}/\text{air}$.

not be measured by CO chemisorption. The catalytic activity is expressed in terms of T_{50} , the temperature at which the conversions of CO, NO and C_3H_6 reach 50% in the light-off of a stream of stoichiometric NO–CO– C_3H_6 – O_2 mixtures ($\text{A/F} = 14.6$). T_{50} of as prepared supported Pd catalysts is dependent on the amount of Fe(x). Although the T_{50} values of as prepared Pd/Fe-10A2B ($x = 1.0$) are lower than Pd/10A2B, further increase of x has negative influences on the catalytic activity. After aging, Pd/Fe-10A2B in the entire composition range ($0 < x \leq 2.0$) were less active than that of Pd/10A2B. The Fe-substitution has therefore no significant improvement for the light-off of stoichiometric NO–CO– C_3H_6 – O_2 mixtures.

The effect of Fe-substitution on the catalytic reactions was further studied under modulated A/F conditions. Fig. 5 exhibits catalytic conversion of CO, NO and C_3H_6 at 390 °C over Pd/10A2B and Pd/Fe-10A2B ($x = 1.0$) when A/F is modulated in the range $13.7 \leq \text{A/F} \leq 15.1$. For each of gas conversions, hysteresis behavior is observed because the catalyst surface should be oxidized to a different extent depending on the direction of A/F scan. Although conversions of CO and C_3H_6 are high at around stoichiometric and lean conditions ($\text{A/F} \geq 14.6$), their conversions in a rich side decreased with decreasing A/F from 14.6 to 13.7. By contrast, NO conversion is high only at round stoichiometric A/F (14.6), but steep drop occurred in the both side. It should be noted that the NO conversion in a rich region ($\text{A/F} < 14.6$) could be improved by the

Table 2
Comparison between Fe K-edge EXAFS analysis and DFT calculation of $\text{Fe}_{1.0}\text{Al}_{19}\text{B}_4\text{O}_{36}$.

Catalyst	Shell	EXAFS		DFT	
		CN ^a (± 0.2)	$r/\text{\AA}^b$ (± 0.03)	CN ^c	$r/\text{\AA}^c$
$\text{Fe}_{1.0}\text{Al}_{19}\text{B}_4\text{O}_{36}$	Fe–O	1.4	1.88	5	1.84, 1.93, 1.93, 1.94, 2.05
	Fe–O	1.9	1.95		
	Fe–O–Al	1.4	2.89	3	2.83, 2.92, 2.92
	Fe–O–Al	1.2	3.26	2	3.36, 3.36
	Fe–O–Al	1.5	3.54	1	3.65
Fe_2O_3	Fe–O	3.0	1.94		
	Fe–O	3.0	2.12		
	Fe–O–Fe	3.0	2.98		
	Fe–O–Fe	3.0	3.35		
	Fe–O–Fe	6.0	3.71		

Interval of k -space to r -space of FT is $3.0\text{--}14.0 \text{\AA}^{-1}$.

^a Coordination number.

^b Interatomic distance.

^c DFT calculation of 5-coordinated Fe on the Al(3) site of 10A2B.

Table 3
Catalytic properties of Pd/Fe_xAl_{20-x}B₄O₃₆.^a

x	As prepared ^b					Aged ^c				
	S _{BET} ^d /m ² g ⁻¹	CO/Pd ^e /%	T ₅₀ ^f /°C			S _{BET} ^d /m ² g ⁻¹	CO/Pd ^e /%	T ₅₀ ^f /°C		
			CO	NO	C ₃ H ₆			CO	NO	C ₃ H ₆
0	70	48	273	285	272	59	4	315	328	313
1.0	44	38	256	258	263	38	0	348	363	343
1.5	19	18	281	281	279	17	0	373	384	369
2.0	12	10	298	294	289	–	–	–	–	–

^a Pd loading is 0.4 wt% as metal.^b Calcined at 600 °C for 3 h in air.^c Aged at 900 °C for 25 h in a stream of 10% H₂O/air.^d BET surface area.^e Metal dispersion of Pd.^f Temperature at which conversion of each gas species reached 50%. 0.05% NO, 0.51% CO, 0.039% C₃H₆, 0.4% O₂/He, A/F = 14.6, W/F = 5.0 × 10⁻⁴ g min cm⁻³, 10 °C min⁻¹.**Table 4**
Catalytic light-off for various elemental reactions.

Reaction	A/F ^a	Pd/Fe-10A2B			Pd/10A2B		
		T ₅₀ ^b /°C			T ₅₀ ^b /°C		
		CO	NO	C ₃ H ₆	CO	NO	C ₃ H ₆
CO–H ₂ O	12.8	379	–	–	479	–	–
CO–O ₂	20.1	146	–	–	129	–	–
NO–CO	14.6	241	248	–	272	282	–
C ₃ H ₆ –H ₂ O	12.8	–	–	518	–	–	402
C ₃ H ₆ –O ₂	15.1	–	–	230	–	–	234
NO–C ₃ H ₆ –O ₂	14.6	–	314	298	–	326	310
NO–C ₃ H ₆	13.3	–	285	439	–	340	456
NO–H ₂	12.8	–	84	–	–	206	–

Concentrations of each gas feed are as follows—CO–H₂O: 0.1% CO, 7% H₂O, He balance; CO–O₂: 0.1% CO, 1% O₂, He balance; NO–CO: 0.1% NO, 0.1% CO, He balance; C₃H₆–H₂O: 0.04% C₃H₆, 10% H₂O, He balance; C₃H₆–O₂: 0.05% C₃H₆, 0.5% O₂, He balance; NO–C₃H₆–O₂: 0.05% NO, 0.04% C₃H₆, 0.15% O₂, He balance; NO–C₃H₆: 0.05% NO, 0.04% C₃H₆, He balance; NO–H₂: 0.05% NO, 0.1% H₂, He balance. W/F = 5.0 × 10⁻⁴ g min cm⁻³, 10 °C min⁻¹.

^a Air-to-fuel ratio calculated for each elemental reactions.^b Temperature at which conversion of each gas species reached 50%.

Fe substitution of 10A2B. Consequently, Pd/Fe-10A2B exhibited a broader active A/F window for NO conversion than Pd/10A2B.

To elucidate the effect of Fe-substitution in a rich region, several elemental reactions were carried out in a light-off mode over Pd/10A2B and Pd/Fe-10A2B. Table 4 summarizes the light-off temperature (T₅₀) for these elemental reactions. The Pd/Fe-10A2B catalyst exhibited higher activities for CO–H₂O, NO–CO, NO–C₃H₆ and NO–H₂ reactions under the stoichiometric and/or rich condition (A/F ≤ 14.6) in accordance with the A/F dependence of the catalytic activity as shown in Fig. 5. Although the NO–H₂ reaction was especially promoted by the Fe-substitution (T₅₀ = 84 °C), the reaction could not occur over Fe-10A2B alone. The promotional effect of Fe is therefore considered to result from interactions between Fe-10A2B and Pd metals under the rich conditions. In the present system, H₂ should be formed by CO–H₂O reaction that requires much higher T₅₀ of 379 °C. However, the concentration of CO (0.51%) about ten times higher than that of NO (0.05%) enables a considerable acceleration of NO conversion by H₂ as a result of the water-gas shift reaction (Fig. 5). In contrast to strong promotional effects on NO–CO and NO–C₃H₆ reactions, apparent CO conversions over two Pd catalysts in a rich region (Fig. 5a and b) are comparable. This is probably because incomplete oxidation of C₃H₆ to CO compensates the consumption of CO by NO–CO and NO–C₃H₆ reactions.

3.3. Redox property of Fe-10A2B

Another possible role of Fe in the structure of 10A2B is associated with the redox and resultant oxygen release/storage properties. Fig. 6 displays the weight change during dynamic oxygen release/storage cycles of Pd/Fe-10A2B and Pd/10A2B under a cycled

feed stream condition (0.7% O₂/N₂ for 40 min and 1.4% H₂/N₂ for 120 min) at 800 °C. On approaching a constant weight in flowing 0.7% O₂ at 800 °C, the gas feed was switched to a mixture of 1.4% H₂. This caused a steep decrease of the weight and subsequent switch to a mixture of 0.7% O₂ immediately gained the weight as was observed before the reduction. In case of unsubstituted Pd/10A2B, a constant weight change of 0.24% is considered as a stoichiometric change between PdO and Pd metal. In case of Pd/Fe-10A2B, however, a larger weight change of 0.72% indicates

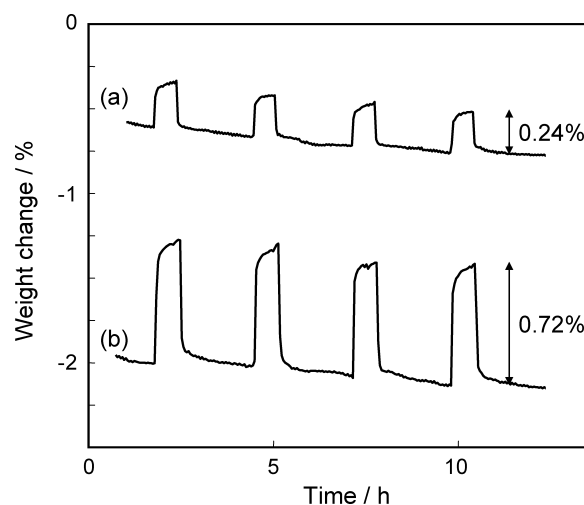


Fig. 6. Weight change during isothermal reduction–oxidation cycles at 800 °C of (a) Pd/10A2B and (b) Pd/Fe-10A2B. Two gas feeds, 1.4% H₂ and 0.7% O₂ balanced by N₂, were switched repeatedly.

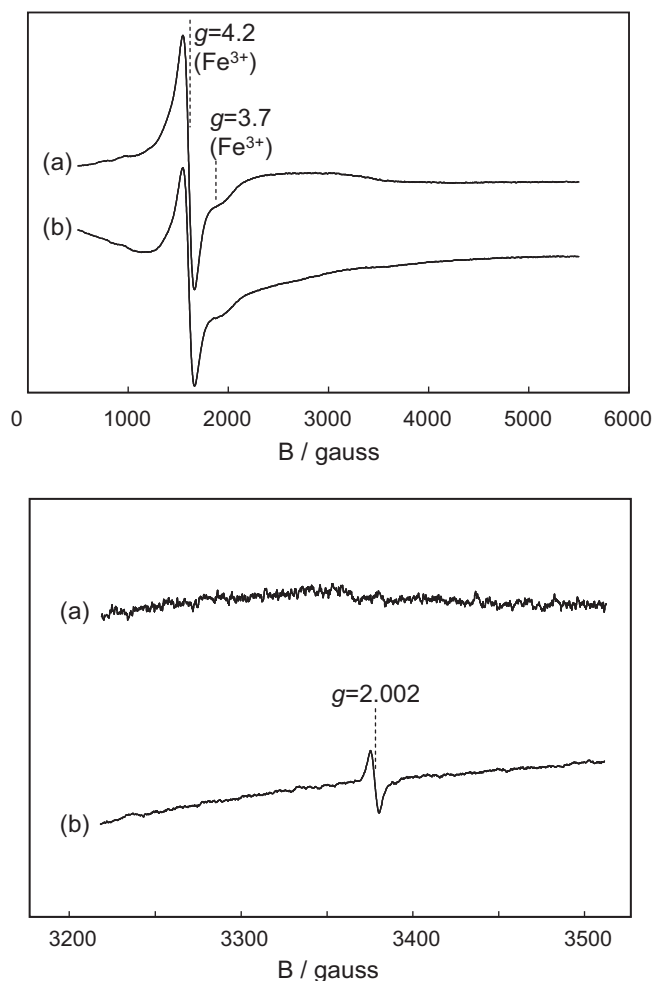


Fig. 7. EPR spectra of Fe-10A2B before and after H₂ reduction at 700 °C. Spectra were recorded at 20 K.

the occurrence of Fe redox, corresponding to the oxygen storage capacity (OSC) of 0.16 mmol-O₂ g⁻¹. This is smaller than the value of 0.23 mmol g⁻¹, which is calculated by assuming the stoichiometric change between Fe³⁺ and Fe²⁺ in Fe-10A2B.

To demonstrate the elimination of lattice oxygen from Fe-10A2B, EPR spectra of Pd-unsupported Fe-10A2B was recorded at 20 K before and after H₂ reduction at 700 °C (Fig. 7). Each spectrum presents signals in magnetic fields less than 2500 gauss that are attributed to isolated Fe³⁺ ions [20,21]. When the deposition of Fe oxide occurs, a wide absorption line should appear above 2500 G due to the dipolar interactions of these ions [22]. But, this is not the case of present Fe-10A2B that contains isolated Fe³⁺ occupying the Al site. The strongest isotropic signal centered at $g=4.2$ are attributed to Fe in rhombically distorted environment, whereas a very weak resonance close to $g=3.7$ corresponds to Fe in more symmetrical site. This is in accordance with the EXAFS and DFT calculation results, which suggest the majority of Fe³⁺ in the 5-coordinated site. The spectrum taken after reduction clearly suggests the decrease of the Fe³⁺ signal at $g=4.2$ accompanied by the appearance of signal at $g=2.002$, which is assigned to paramagnetic oxygen vacancy [23,24]. Consequently, the weight change of Pd/Fe-10A2B in Fig. 6 can be explained by the redox between Fe³⁺ and Fe²⁺ accompanied by reversible sorption/desorption of lattice oxygen.

Finally, the A/F buffering effect of Fe-10A2B at 500 °C was evaluated using simulated gas streams under A/F perturbation conditions (Fig. 8). When the two simulated gas feeds with A/F = 15.0 and 14.2 were switched periodically with an interval of 10 s (dashed

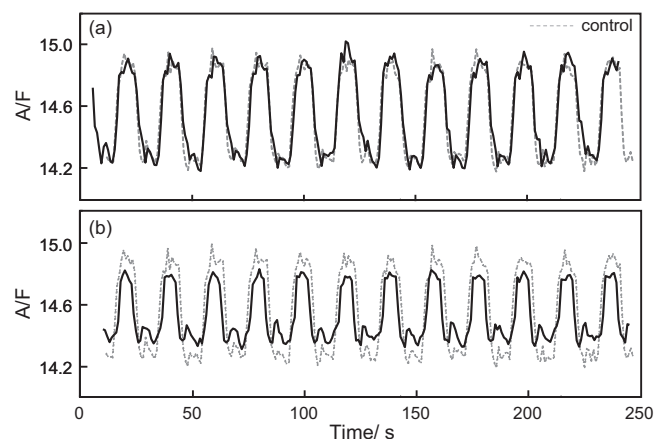


Fig. 8. A/F buffering effect of (a) 0.4 wt% Pd/10A2B and (b) 0.4 wt% Pd/Fe-10A2B ($x = 1.0$) during perturbation between rich and lean simulated gases at 500 °C. Lean (A/F = 15.0): 0.0525% NO, 0.5% CO, 0.04% C₃H₆, 0.83% O₂, 7% H₂O, He balance; rich (A/F = 14.2): 0.0525% NO, 0.5% CO, 0.04% C₃H₆, 0.17% O₂, 7% H₂O, He balance; interval = 10 s.

line), the evolutions of A/F after the catalyst bed (solid line) versus the time on stream were recorded. These two lines are almost identical in case of Pd/10A2B, suggesting a negligible buffering effect. By contrast, the amplitude of oscillation is clearly reduced by Pd/Fe-10A2B in accordance with the higher OSC. Fe-10A2B is therefore able to mimic the function of CeO₂ and/or CeO₂-ZrO₂ oxygen scavengers in automotive three-way catalyst systems.

4. Conclusion

The present study has demonstrated that Fe-substituted 10A2B is promising as a multifunctional support material for automotive Pd catalysts. Among various transition metal cations, Fe is found to be most easily accommodated in the 10A2B structure. Solid solutions can be formed at $x \leq 1.5$ in Fe_xAl_{20-x}B₄O₃₆ without impurity phases. Fe-K-edge EXAFS and DFT calculation suggest that Fe tends to occupy the 5-coordinated Al site rather than tetrahedral and octahedral sites. Catalytic tests in a light-off mode and in a modulated A/F mode conclude that Fe-10A2B can play a key role not only in promoting NO_x reduction under the rich condition (A/F < 14.6), but also in yielding oxygen release/storage capacity, which achieves an efficient buffering effect on the A/F oscillation.

Acknowledgements

This study was supported by Elements Science and Technology Project from the Ministry of Education, Culture, Sports, Science and Technology. XAFS experiments were carried out on BL-7C of Photon Factory (PF), High Energy Accelerator Research Organization (KEK) (Proposal No. 2011G619).

Appendix A. Supplementary data

Supplementary data associated with this article can be found, in the online version, at <http://dx.doi.org/10.1016/j.apcatb.2013.04.010>.

References

- [1] K. Ikeue, S. Hinokuma, K. Watanabe, T. Minekishi, T. Sato, Y. Nakahara, M. Machida, Bulletin of the Chemical Society of Japan 85 (2012) 468.
- [2] E.V. Sokolova, A.V. Azizov, M.A. Simonov, N.I. Leoniuk, N.V. Belov, Doklady Akademii Nauk SSSR 243 (1978) 655.
- [3] M. Fisch, T. Armbruster, D. Rentsch, E. Libowitzky, T. Pettke, Journal of Solid State Chemistry 184 (2011) 70.

- [4] H.N. Baumann, C.H. Moore, *Journal of the American Ceramic Society* 25 (1942) 391.
- [5] H. Scholze, *Zeitschrift für anorganische und allgemeine Chemie* 284 (1956) 272.
- [6] R. Abbas-Ghaleb, E. Garbowski, A. Kaddouri, P. Gelin, *Catalysis Today* 117 (2006) 514.
- [7] M. Machida, K. Eguchi, H. Arai, *Journal of Catalysis* 120 (1989) 377.
- [8] M. Machida, K. Eguchi, H. Arai, *Journal of Catalysis* 123 (1990) 477.
- [9] H. Arai, M. Machida, *Catalysis Today* 10 (1991) 81.
- [10] H. Arai, M. Machida, *Applied Catalysis A-General* 138 (1996) 161.
- [11] H. Inoue, M. Machida, K. Eguchi, H. Arai, *Journal of Materials Chemistry* 6 (1996) 455.
- [12] K. Sekizawa, K. Eguchi, H. Widjaja, M. Machida, H. Arai, *Catalysis Today* 28 (1996) 245.
- [13] K. Sekizawa, M. Machida, K. Eguchi, H. Arai, *Journal of Catalysis* 142 (1993) 655.
- [14] G. Kresse, D. Joubert, *Physical Review B* 59 (1999) 1758.
- [15] H.J. Monkhorst, J.D. Pack, *Physical Review B* 13 (1976) 5188.
- [16] S.L. Dudarev, G.A. Botton, S.Y. Savrasov, C.J. Humphreys, A.P. Sutton, *Physical Review B* 57 (1998) 1505.
- [17] V.I. Anisimov, J. Zaanen, O.K. Andersen, *Physical Review B* 44 (1991) 943.
- [18] G.D. Gatta, N. Rotiroti, M. Fisch, T. Armbruster, *Physics and Chemistry of Minerals* 37 (2010) 227.
- [19] H. Tanaka, F. Hirotoshi, I. Takahashi, *SAE Paper* (1995) 950256.
- [20] K.C. Lombardi, A.S. Mangrich, F. Wypych, U.P. Rodrigues-Filho, J.L. Guimarães, W.H. Schreiner, *Journal of Colloid and Interface Science* 295 (2006) 135.
- [21] C.R. Budziak Fukamachi, F. Wypych, A.S. Mangrich, *Journal of Colloid and Interface Science* 313 (2007) 537.
- [22] E. Guimarães, A.S. Mangrich, V.G. Machado, D.G. Tragheta, M.A. Lobo, *Journal of the Brazilian Chemical Society* 12 (2001) 734.
- [23] J.M. Smith, W.E. Vehse, *Physics Letters A* 31 (1970) 147.
- [24] W.L. Warren, M.R. Shaneyfelt, D.M. Fleetwood, J.R. Schwank, P.S. Winokur, R.A.B. Devine, *IEEE Transactions on Nuclear Science* 41 (1994) 1817.